

Ice loads and deformations of the fixed quay in Spitsbergen

Marchenko, A. ¹, Marchenko, N. ¹, Visich, A. ^{1,2}, Podlesnych, S. ³

¹The University Centre in Svalbard, Longyearbyen, Norway

²Moscow Institute of Physics and Technology, State University, Dolgoprudny, Russia

³Prokhorov General Physics Institute, Moscow, Russia

ABSTRACT

Fixed quay in Kapp Amsterdam was constructed near Svea mine in the Van Mijen Fjord in Spitsbergen in 2000. The paper presents results of the field investigations of the deformations of structural elements of the quay, measurements of ice stresses near the quay cofferdam, and observations of ice processes near the quay. Maximal ice stresses were recorded in syzygy tide at the stage of low tide. Sea water floods at the ice surface near cofferdam were discovered in syzygy tide at the stage of high tide. Numerical simulations were performed to investigate the influence of the water floods on thermal stresses in sea ice at the stage of low tide.

KEY WORDS: Fixed quay, Deformations, Thermal stresses, Tide

INTRODUCTION

The coal quay in Kapp Amsterdam located in the Van-Mijen Fjord (Spitsbergen) was designed and reconstructed in 2000 by AF Anlegg Harbour for loading operations on vessels with dead weights up to 70 000 t (Fig. 1). The total length of the quay is 195 m, it is keyed in the seabed with vertical piles of 80 cm diameter and steel joggle skirts (JS) connecting the piles of three cofferdams. Plane view of two cofferdams on the East side of the quay is shown in Fig. 2a. Soil was added at the bottom inside the cofferdams. The difference between water depths on sea side of the quay and inside cofferdams is of about 10 m. The mean water depth inside cofferdams is around 5 m. Sea water penetrates through the skirt, and in ice-free season the water levels inside and outside the skirts are the same (Marchenko et al, 2011).

Significant deformations of JS in alongshore direction were registered in the quay cofferdams since 2008, while deformations of JS in onshore direction were smaller (Sinitsyn et al., 2012). Progressive deformations of the skirts in alongshore direction were prevented by welding of steel holders between the skirt and the horizontal beams welded to the vertical piles. Visual observations of different behavior of ice trapped inside the JS and ice floating outside JS indicated that ice load is a reason for the observed deformations of JS.

Depending on the moon phase the height of semidiurnal tide changes from 1 m to 2 m in the Van-Mijen fjord (Kowalik et al, 2015). Sea ice outside JS moves up and down together with sea water due to the tide. The ice trapped inside cofferdams is frozen to JS and follows the water motion by bending. Tide induced overpressure inside cofferdams influences floods on

the ice surface caused by water migration through the ice. The floods were observed systematically in high tide when the tide amplitude was big enough. In low tide the ice was hanging on JS, and the middle part of the ice sheet displaced downward up to 0.6 m in comparison to high tide. Bending deformations of ice influence mechanical loads on JS. Changes of ice temperature due to water migration through the ice (Wrangborg et al, 2015) influence thermo-mechanical loads on JS.

Ice pressure on JS and ice temperature were recorded over two winter seasons in 2013 and 2015 (Marchenko, 2018). Temperatures of the air, ice, and water were recorded with spatial resolution of 0.2 m by temperature string mounted on the vertical piles inside the right cofferdam in Fig. 2a. Temperature fluctuations in the upper layer of ice were measured of about 1°K and lower. Temperature of bottom layer of ice, and water temperature were at the freezing point ($\sim -2^\circ\text{C}$). Ice pressure magnitudes were below 0.2 MPa in most of the records except the record of ~ 100 h duration in April 2013 when pressure magnitude exceeded 0.4 MPa and its maximum reached to 0.6 MPa. Spectrums of the pressure records corresponded to tide constituents M2, M4 and 2M6 with periods 12.42 h, 6.2 h, and 4.1 h. Correlation analysis shows that highest pressures of the surface ice layer on JS are realized in high tide except the 100 hours record in April 2013 when highest pressures of the surface ice layer on JS were recorded in low tide.

Linear coefficient of thermal expansion of freshwater ice is of about $\text{CTE}=5\cdot 10^{-5}\text{ K}^{-1}$ (Pounder, 1965). Thermal loads caused by variations of the ice temperature with amplitude of 1°C lead to ice pressures on JS up to 0.1 MPa when the ice trapped inside JS expands as freshwater ice and its elastic modulus is 2 GPa. Numerical simulations with the elasticoplastic model of ice estimated pressure amplitude below 0.15 MPa when the ice temperature changes according to the 100 h temperature records in April 2013 (Marchenko, 2018). The increase of ice pressure in the surface ice layer up to 0.6 MPa in low tide was reproduced by numerical simulations with the elasticoplastic model of ice and negative effective coefficient of thermal expansion $\text{ECTE}=-5.5\cdot 10^{-4}\text{ K}^{-1}$.

Measurements of ice stresses on the marine side of the quay have been performed in this area earlier. Instanes (1979) made measurements in connection with the construction of the coal quay in the area. Moslet (2001) also measured stresses close to the same quay to estimate ice loads. Stresses up to 42.8 kPa were measured at 0.2 m depth from February to May 2002 close to the quay. This stress peak was caused by thermal expansion. A good relationship between semi-diurnal stress variations and the water level fluctuations (the tide) has been found. The ice cover was in some way deformed in bending, but the exact pattern of deformation and the reason for it are still indistinct (Moslet and Hoyland, 2003). Two events of ice pressure increase above 0.9 MPa and 1.3 MPa were recorded on the sea side of JS in the beginning of May 2013 (Marchenko, 2018). Except for these two high pressure events the ice pressure with less than 2 h durations the recorded ice pressures oscillated with semidiurnal frequency, and the ice pressures on the sea side of the JS were lower 50 kPa. It was unclear if these two high-pressure events on the sea side of the JS are associated with thermal or mechanical loads from ice. Maximal ice pressure of 1.2 MPa was also recorded on the Nanisivk Wharf (Poirier et al, 2019). In winter 2015 four events of ice pressure above 50 kPa were registered. The recorded in high tide pressures were 280 kPa, 100 kPa, 150 kPa, and 180 kPa.

Depending on the tide amplitude floods were observed in the hinge zone in high tide. In low tide the surface of hinge zone was dry. Usually, two cracks are well visible in the hinge zone. Ice blocks between the cracks are bent and rotated over the tidal cycle. In ice free season it was discovered that JS section on the marine side of the quay cyclically moves by wave action with the amplitude of about few centimeters (Marchenko, 2018). In the present paper we analyze mechanical loads on JS, compare and analyze deformations of the JS of the coal quay recorded

in 2020 with the deformations earlier measured in the same place. The results of the measurements of ice pressure on the marine side of the JS are described, and the influence of water floods on thermal expansion of sea ice is investigated.

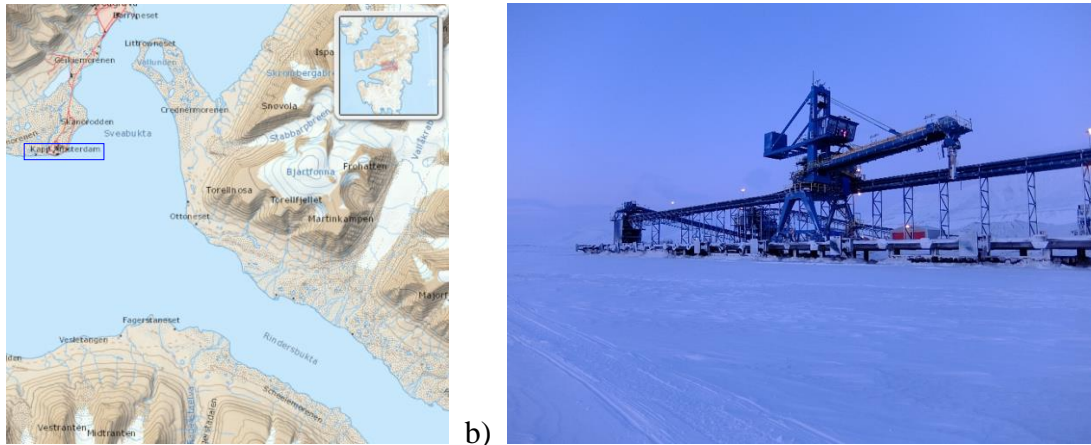


Figure 1. Location (a) and photograph (b) of Coal quay in Kapp Amsterdam in Spitsbergen.

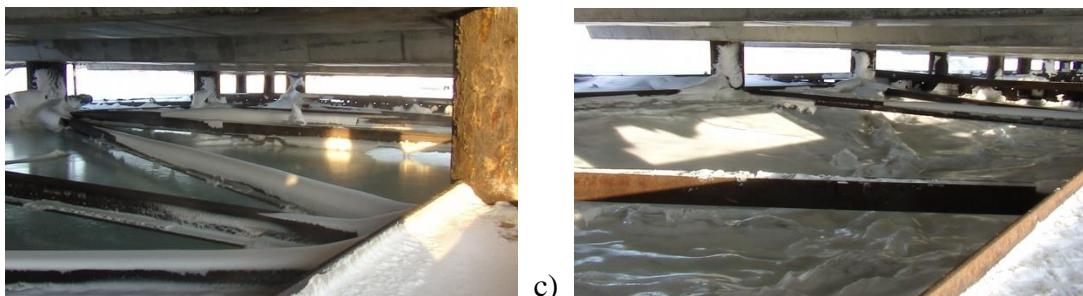
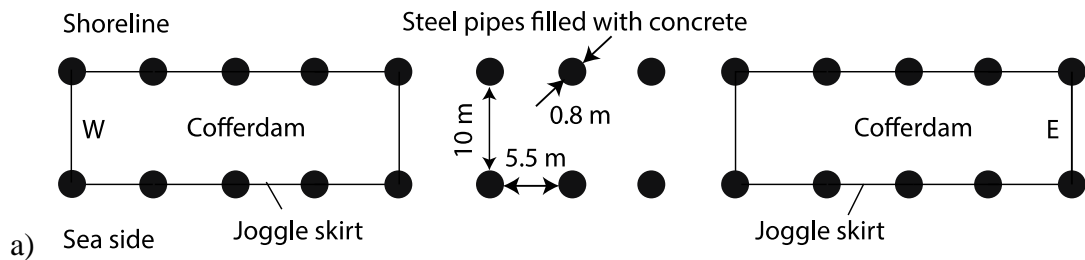


Figure 2. Scheme of structures supporting the quay (a). Sea ice inside JS in high (a) and low (c) tide. Photographs of the author (2013).

MECHANICAL LOADS OF ICE ON JOGGLE SKIRT

Deforming of ice and formation of ice loads on JS skirt during high and low tides due to pure mechanical processes is illustrated in Fig. 3a. Observations show significant vertical displacements of the ice in the middle of cofferdams, while the ice frozen to JS is not moving. These bending deformations of the ice influence ice failure inside cofferdams. Narrow zones where the ice surface is not smooth are visible in low tide (Fig. 2b). Spatial locations of these narrow zones are shown by lines in Fig. 3b. It is natural to assume that these lines mark places of ice faults. Ice blocks separated by the faults rotate and displace relatively each other over the tidal cycle. The blocks are never separated from each other when the ice thickness is big enough. Small cracks between the blocks are filled by brine and frozen very fast. Sea water migrates upward through channels inside ice the faults and through the solid ice when the water pressure below the ice increases.

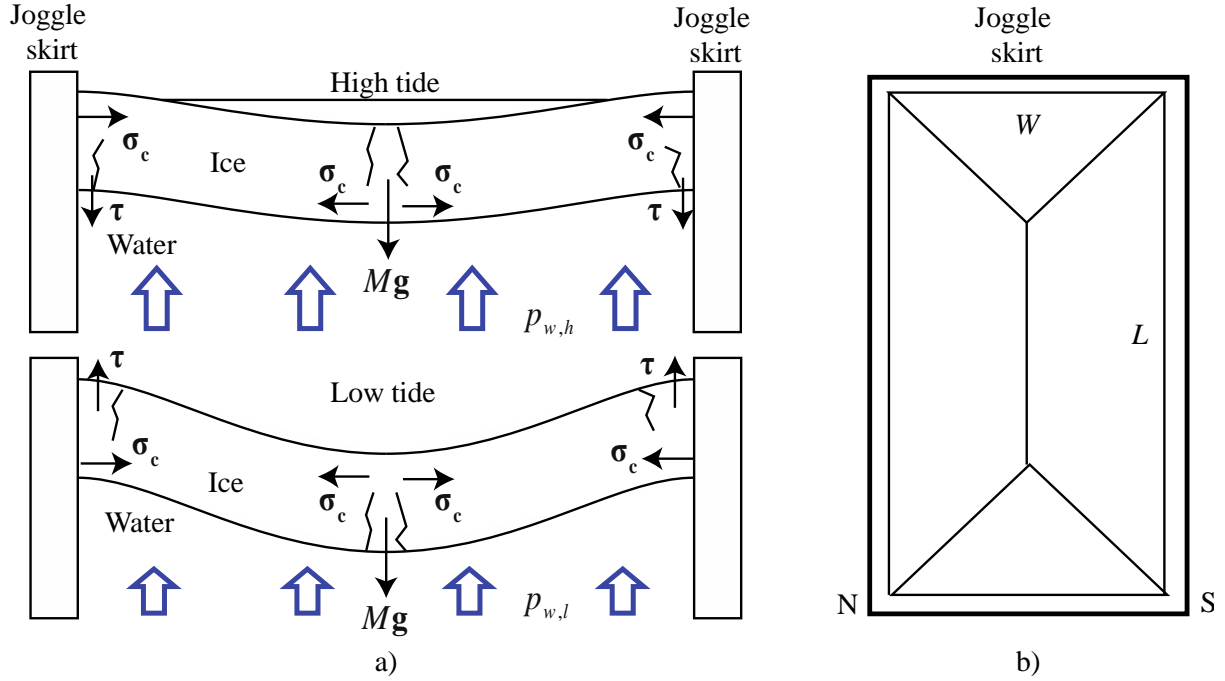


Figure 3. Schematic of the formation of mechanical ice loads on JS during high and low tides (a). Configuration of ice faults on the ice surface inside JS observed in low tide (b).

Balance of forces applied to the ice in the vertical direction is written as follow

$$2\tau h_i(L + W) = \int_{S_b} p_w dS - (M_i + M_f)g, \quad (1)$$

where τ is the shear stress averaged over the lateral surface of ice frozen to JS, L and W are the horizontal dimensions of the ice sheet inside JS (Fig. 3b), h_i is the ice thickness, M_i is the mass of the ice sheet, M_f is the mass of flood water on the ice surface, S_b is the surface of the ice bottom, p_w is water pressure below the ice, and g is the gravity acceleration. The mass of the ice sheet is calculated with the formula $M_i = \rho_i h_i L W$, where ρ_i is the ice density.

The integral in (1) can be estimated in low and high tide with the assumptions that $p_w = \rho_i g h_i$ in high tide, and $p_w = 0$ in low tide. The estimates are valid when the ice is frozen to JS. According to these assumptions the absolute shear stresses in low and high tides satisfy to the inequalities

$$|\tau| \leq \tau_h, \quad \tau_h = g L W \frac{(\rho_w - \rho_i) - \rho_w h_f / h_i}{2(L+W)} \quad \text{in high tide}, \quad (2)$$

$$|\tau| \leq \tau_l, \quad \tau_l = \frac{\rho_i g L W}{2(L+W)} \quad \text{in low tide}. \quad (3)$$

The dimensions of JS are $L = 20$ m, and $W = 10$ m. The mean depth of water flood on the ice surface in high tide is of about $h_f = 20$ cm, and the mean ice thickness $h_i = 2$ m (Marchenko et al., 2011). Assuming ice and water densities equal to $\rho_i = 930$ kg/m³ and $\rho_w = 1030$ kg/m³ we find the estimates $\tau_h \approx 743$ Pa, and $\tau_l \approx 30$ kPa. Thus, the shear stress at low tide is much greater the shear stress at high tide.

Normal compressive stresses (σ_c) on JS can be estimated using the friction law $\tau = \mu \sigma_c$ when

the ice is not frozen to JS and may slide along JS. The static coefficient of friction of ice with corroded steel was estimated in the range $\mu \in (0.2, 0.5)$ (Milano, 1973; Rivlin, 1973). It leads to the estimate $\sigma_c < 0.15$ MPa for the compression at low tide.

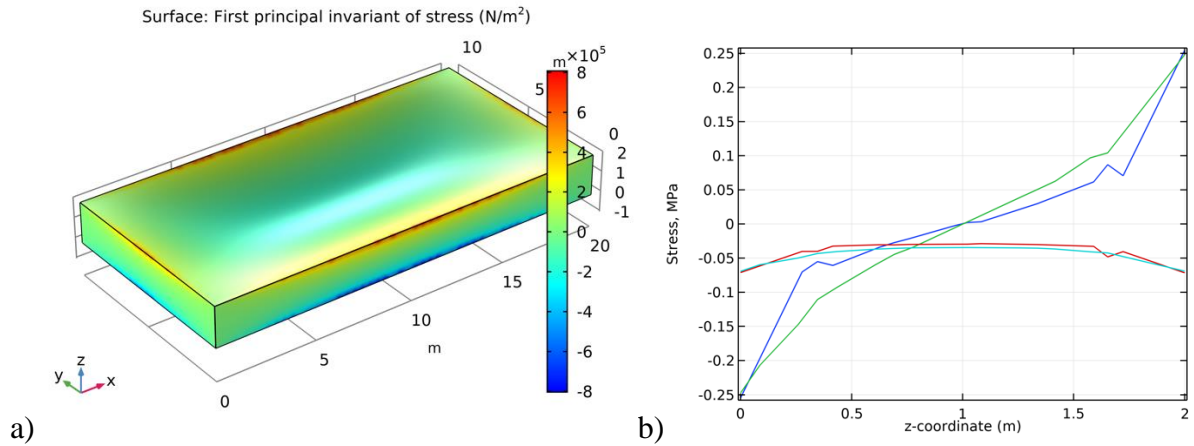


Figure 4. First stress invariant at the surface of hanging ice plate (a). Stresses σ_{xx} (blue line) and σ_{xz} (red line) in the middle of JS edge of the length W ; stresses σ_{yy} (green line) and σ_{yz} (aquamarine line) in the middle of JS edge of the length L (b).

Numerical simulations were performed by finite element software Comsol Multiphysics to calculate ice stresses on the walls of JS shown in Fig. 3 with $L = 20$ m and $W = 10$ m at low tide when the ice is hanging on JS walls. The ice thickness was set to 2 m. Pure elastic material with the elastic modulus of 2 GPa and Poisson's ratio of 0.35 was used to model ice in the simulations. Figure 4a shows the shape of the ice plate and distribution of the first stress invariant over the ice surface. The ice pressure is smaller the invariant in 3 times and has opposite sign. Its maximal value reaches 0.26 MPa. Figure 4b shows normal and shear stresses at the ice edges. Maximal compression stress reaching 0.25 MPa realizes near the ice bottom at $z = 0$. The mean shear stress is lower 50 kPa. It is evident that mechanical deformations can't explain ice pressure on JS up to 0.6 MPa in surface layers of ice at low tide.

DEFORMATION ANALYSIS OF JOGGLE SKIRTS

Seven laser scanning sessions with various scan positions and modes were performed to find out deformations of cofferdam constructions since January 2012. In March 2020 the most detail survey was implemented with 22 scans from positions surrounding cofferdam (Fig. 5a). Terrestrial Laser scanner Reigl VZ 1000 gave point clouds with resolution of several millimeters. Processing of point clouds (adjustment of scan positions and filtering) in special software (RiScan Pro and CloudCompare) allowed to see the difference, measure the distance between locations of the same elements in various time and determine offset shift. The results are shown in Fig. 5b (all three cofferdam constructions) and Fig. 6 (central part zoomed), where yellow is for points of scanning in January 2012 and other colors are for scanning in March 2020. Fig. 5 and Fig. 6 are oriented traditionally – West is on the left side, the cofferdam parts can be numbered also from left (west) to the right (east).

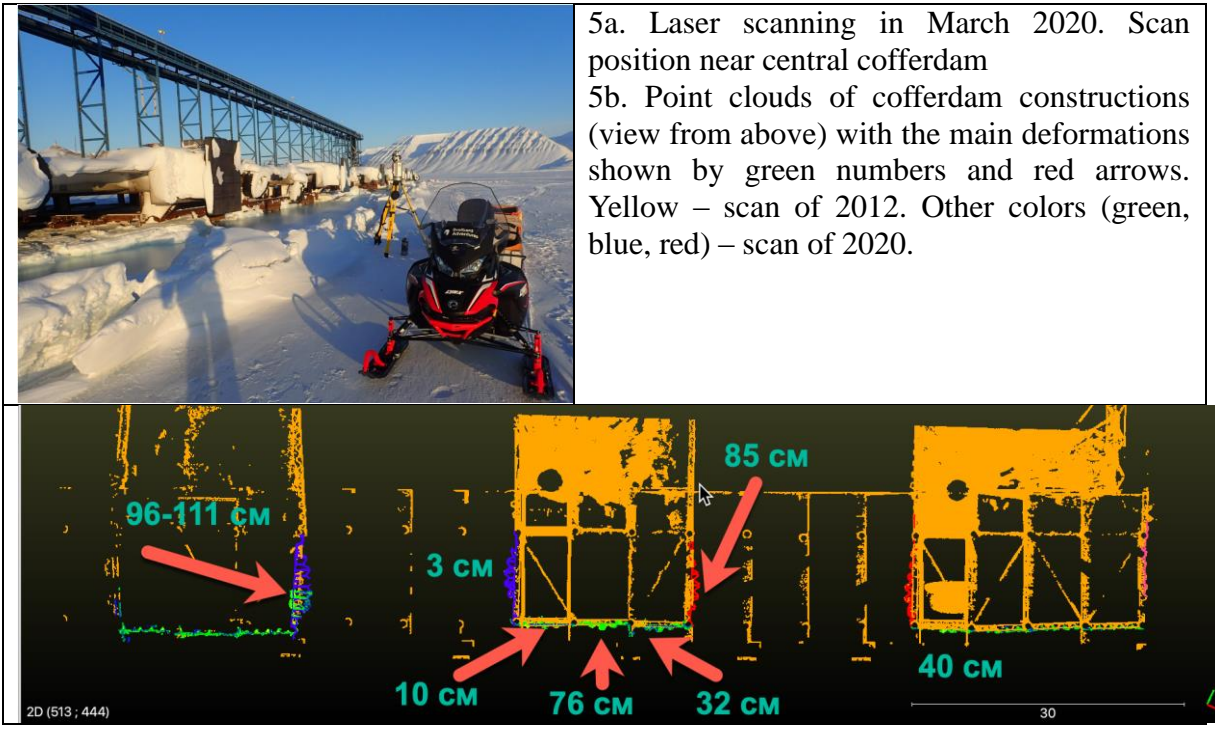
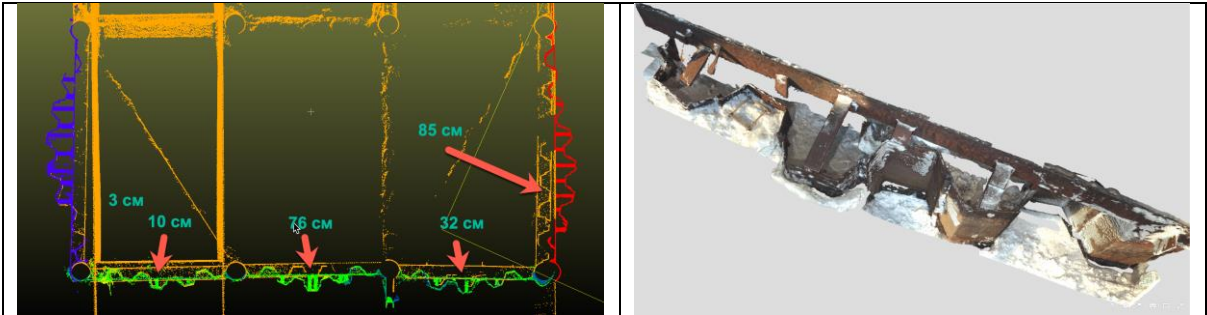


Figure 5. Laser scanning procedure and results

Figure 6 provides the most graphic representation of the point clouds (Fig. 6a) and 3D model (Fig. 6b) and shows how the JS have been shifted under ice pressure over 8 years. Fig. 6 shows the central cofferdam. The 3D model is made by combining of multi photo images. Here the deformations and ruptures of metal reinforcement are obvious. The first western cofferdam is the most deformed. Even on the 2012 scan, it can be seen that it was swollen like a keg. In 2020, the situation worsened and on the eastern wall the differences between 2012 and 2020 reach 111 cm.

The third eastern cofferdam is the best preserved. In it, only the extreme western segment of the frontal part led by 40 cm. The side walls were practically unchanged. The second central cofferdam is significantly deformed on the eastern wall (85 cm) and the central part of the frontal (up to 76 cm) (Fig. 6a). On the western wall, deformations are insignificant (3 cm). It is obvious (see also Fig. 6b) that efforts were being made by maintaining company to stop the bulging - iron bars/strips were welded on. But there are many places, where there are no contours, the strips are torn off or sawed off.



6a. Point clouds of central cofferdam (view from above). Yellow – scan 2012. Other colors (green, blue, red) – scan 2020. Green numbers are shift over 8 years in particular places (red

6b. 3D Models of the right part of central cofferdam. The model can be seen and explored on <https://sketchfab.com/3d-models/kapp-amsterdam-cofferdam->

arrows).

[6c752133a17541c3a097ba2be7aa73de](#))

Figure 6. Deformation of central cofferdam

ICE PROCESSES NEAR KAPP AMSTERDAM COAL QUAY

Field works near the coal quay in March 2020 included measurements of ice pressure with pressure cells Geokon, measurements of ice thickness by drilling, measurements of ice salinity and ice temperature. Time laps camera Reconix was mounted on the quay to make shots with sampling interval 5 min for monitoring of ice motion. Pressure and temperature recorder SBE-39 was deployed at sea bottom near the JS to measure water level elevation by tide versus the time. The measurements were performed near the cofferdam 2, where pressure cells were installed in 2013-2015. Maximal ice thickness inside the cofferdam reached 4 m. The ice thickness profile from marine side of the cofferdam is shown in Fig. 7. The ice thickness between the cofferdam and tidal crack was changing between 1 m and 3 m. The tidal crack was extended from the JS on approximately 7.5 m. Ridge keel was discovered at 4 m distance from the JS. The level ice thickness outside the crack was near 1 m.

The time laps camera registered vertical displacements of ice between the JS and the tidal crack. They were smaller than the vertical displacements of level ice over tidal cycles. Vertical displacements of level ice on several meter distance from the tidal crack were similar the water level elevation due to semidiurnal tide. The ice edges near the tidal crack were destroyed and small ridge sail extended along the crack (Fig. 7a). The ice surface between the JS and the tidal crack had negative slope in offshore direction in low tide (left panel in Fig. 7b). In high tide this ice surface had positive slope in offshore direction. Tidal amplitude changed according to the moon phase, and the slope angles of the ice surface increased with increasing tide amplitude. The entire ice block was moving up down along JS together with water, but the amplitude of this motion was smaller the tidal amplitude (Fig. 7b). In addition, bending deformations of ice were visible near the ice crack. Sea water floods formed at the surface of ice between the JS and the crack when the tide amplitude was relatively high. Photographs in Fig. 8 show that sea water was coming at the ice surface along the wall of JS.

Similar floods were earlier observed inside the cofferdam (Wrangborg et al, 2015; Marchenko, 2018). In 2020 ice thickness inside the cofferdam was large and floods didn't form. Inside the cofferdam sea water penetrated on the ice surface in central part of the cofferdam in contrast to the floods from marine side of the JS. The ways of water migration through the thick ice inside the cofferdam were not evident. Sea water brine can migrate by brine channels and by ice cracks.

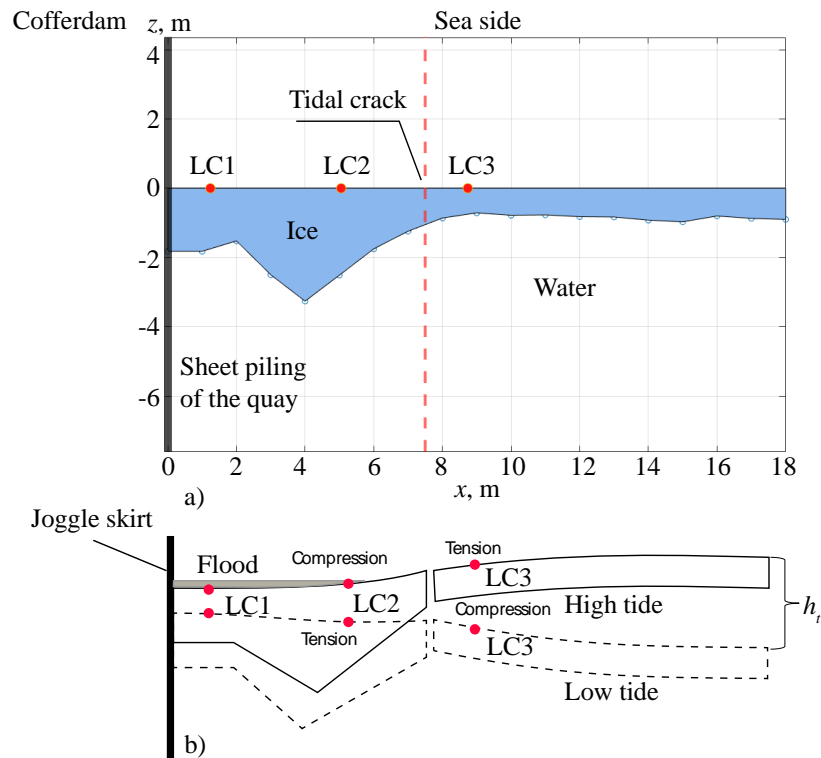


Figure 7. Ice thickness profile over 18 m distance from the sea side of the cofferdam 2. Locations of ice pressure cells are marked LC1, LC2, and LC3 (a). Schematics of ice cover shape in low and high tides (b).

The maximum depth of the floods in March 2020 was measured about 30-40 cm. The temperature of the water coming out of the cracks was measured with a contact thermometer several times in different places and was found to range from -1.9°C to -2.1°C , which implies fast supercooling of the water. When water samples were collected into plastic boxes to measure the salinity afterwards it was visible how initially clear water was rapidly becoming slushy from the small crystals of ice forming in it. The salinity of the water was measured to be equal to 33 ppt, and the salinity of slush and new ice formed from flood water was measured in the range of 19-26 ppt.

Geokon pressure cells were placed in the cuts made in the ice by chain saw. Initially they were placed at the depth of about 25 cm, and frozen in the ice by adding of fresh water at the freezing point into the cuts. After several floods the ice surface was growing upward due to the formation of new ice, and the distance of the pressure cells from the ice surface became bigger. Ice pressures recorded versus the time are shown in the top panel of Fig. 9. Semidiurnal dependence of the pressures versus time is clear visible. The pressure amplitudes increased with increasing of tidal amplitude shown in the bottom panel of Fig. 9. Phase shifts between the stresses recorded by LC1 (blue line), LC2 (brown line), and LC3 (green line) are well visible in the records on March 05-09. The floods were much smaller and shorter in this period of observations. Pressure phases recorded by LC1 and LC3 were better synchronized on March 11-12, when the tidal amplitude was maximal, and the floods formed near JS. LC1 recorded highest pressures at low tides, and maximal pressures are associated with the times of floods formation.



Figure 8. Photographs of time laps camera in low tide (left) and high tide (right).

Figure 9 shows that LC2 recorded maximal pressures when LC3 showed minimal pressures and v.v. on March 05-09. Figure 7b explains time shift between high compressions measured by LC2 and LC3 by ice bending. The curvature of ice surface had different sign from different sides of the tidal crack. Pressure cells measured high compression in case of maximal positive curvature of the ice surface. Pressure cells didn't measure tensile stresses in case of negative curvature. Similar arguments explain smaller phase shifts between maximal pressures measured by LC1 and LC2.

LC1 recorded maximal pressures at low tides, and the amplitudes of the pressures increased significantly in syzygy tide on March 11-12, when the floods formed in high tide. We think that thermal expansion of ice can explain the high pressures. Thermal expansion was caused by the cooling of ice surface when sea level and sea water flux into the ice and on the ice surface decrease. Some amount of brine becomes trapped inside ice due to ice compression at high tide and freezes when sea water level goes down. Influence of ice compression on the permeability was discussed by Renshaw et al (2018). Two local maxima of the pressure measured by LC1 on March 11-12 are related to mechanical compression by high tide and thermal compression by low tide. Similar effects were observed inside the cofferdam (Marchenko, 2018).

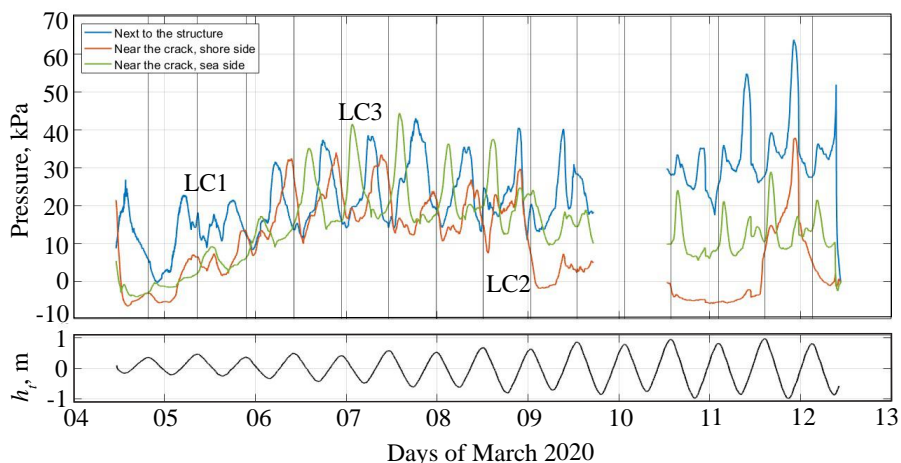


Figure 9. Records of ice pressure cells versus the time (top panel), and tidal elevation of the water level versus the time (bottom panel).

NUMERICAL SIMULATIONS

Numerical simulations were performed in Comsol Multiphysics software to investigate the influence of surface water floods on thermal expansion of ice. Moduli Solid Mechanics, Heat Transfer in Solids, and Multiphysics were used. Plane strain approximation with the thickness of computational domain 100 m were used. The computational domain was a rectangle with horizontal size of 5 m ($x \in (0,5)$) and vertical size of 1 m ($y \in (0,1)$) (Fig. 10). Linear isotropic elastic model with creep was used to describe ice rheology. The elastic modulus, Poisson's ratio and density were respectively 2 GPa, 0.33, and 910 kg/m³. The creep was described by the Norton model with reference stress of 1 MPa, reference strain rate of 10⁻⁶s⁻¹, and stress exponent of 3. The upper and bottom surfaces of the rectangle were free from the loads, and zero displacement were set at the edges of the rectangle at $x = 0$ and $x = 5$.

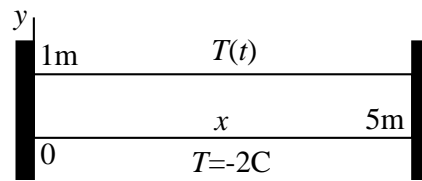


Figure 10. Computational domain.

Temperature at the bottom of the rectangle was set to -2°C. The surface temperature changed between -2°C and -20°C with semidiurnal period of 12.42 h. The change of the surface temperature with time was described by the wave form shown by blue lines in Fig. 12. The condition of thermal insulation was set at the edges of the rectangle at $x = 0$ and $x = 5$. The thermal conductivity was set to 1.8 W/m·K. The specific heat capacity of fresh ice was set to 2 kJ/kg·K, and the linear coefficient of thermal expansion of fresh ice was set to 5·10⁻⁵ 1/K. Figure 11 shows the dependencies of the specific heat capacity and the linear coefficient of thermal expansion from the temperature used in numerical simulations of sea ice. They correspond qualitatively to the dependencies found in the experiments (Schwerdtfeger, 1963; Nazintcev, 1964; Marchenko and Lishman, 2017).

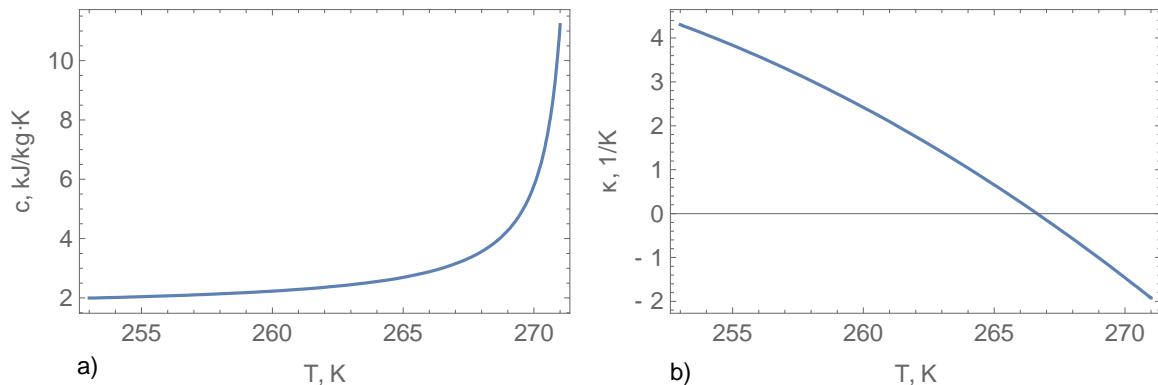


Figure 11. Dependencies of the specific heat capacity (a) and the linear coefficient of thermal expansion (b) from the temperature used in numerical simulations of sea ice.

Results of numerical simulations are shown in Fig. 12 and Fig. 13. The left and right panels correspond to sea ice and fresh ice. One can see that the amplitudes of horizontal stresses in the middle of the rectangle ($x = 2.5$) decrease with the distance from the surface of the rectangle. The stress amplitudes shown in Fig. 12a are about 30 kPa on the aquamarine line, and about 15 kPa on the red line. It corresponds well to the range of stress changes in Fig. 9 on

March 11-12. Stress variations near the ice surface are much greater in fresh ice, where large compressions are alternated with large tensions (Fig. 12b). The last property influences smaller reaction forces at the edges of the rectangle in case of fresh ice (right panel in Fig. 13b). It is of interest that the reaction forces (compression) at the edges of sea ice are higher but appear only over short times when the temperature rates are high (Fig. 13a).

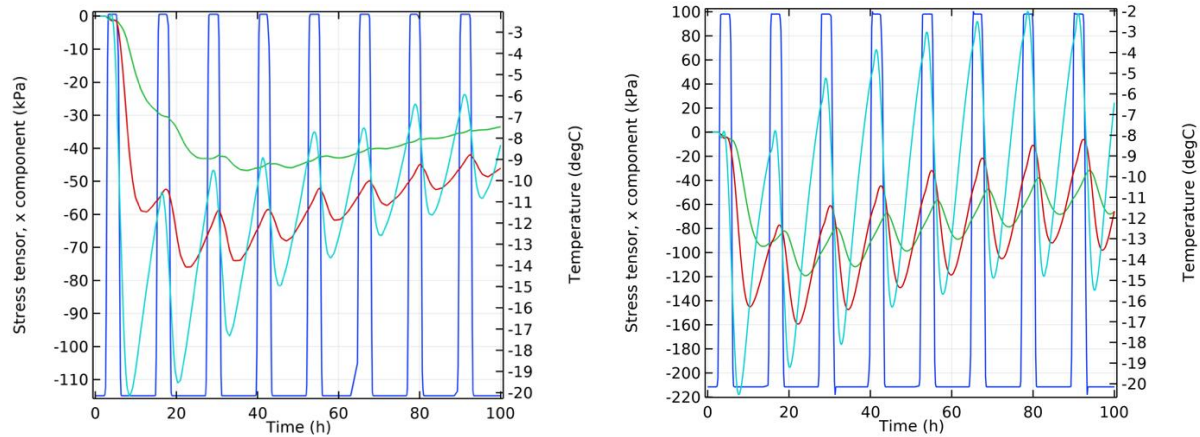


Figure 12. Results of numerical simulations with models of sea (left panel) and fresh (right panel) ice. Temperature (blue line), and stresses in the middle of the ice plate at the depths 0.3 m (aquamarine line), 0.4 m (red line), and 0.5 m (green line) versus time.

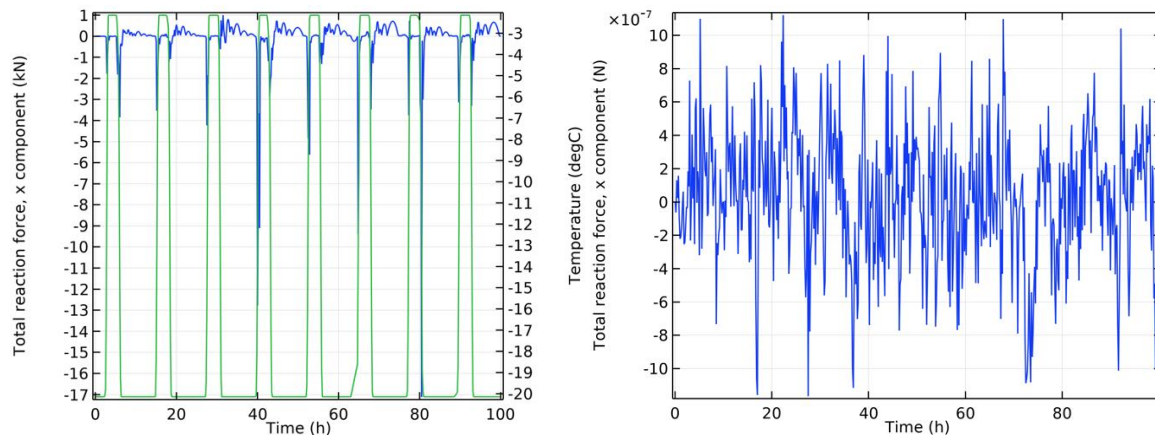


Figure 13. Results of numerical simulations with models of sea (left panel) and fresh (right panel) ice. Temperature (green line), and reaction force on the ice edge (blue line) versus time.

ESTIMATES OF WAVE LOADS

In ice free season storm waves acts on the cofferdam. Wave loads over unit length of cofferdam can be estimated with the formula (Oumeraci et al., 2001)

$$F_w = 15\rho_w g H^2 (H_{sw}/H)^{3.134}, \quad (4)$$

where H is the water depth, and H_{sw} is significant wave height.

Wave characteristics were estimated in Svea Bay located to the North-East of the quay (Fig. 1a). Significant wave height below 0.8 m with peak period of 3.4-3.5 s were calculated with assumption that the fetch is 10-13 km. The fetch near Kapp Amsterdam is estimated of about

40 km for South-East winds blowing along Rindersbukta (Fig. 1a). Then, significant wave height is of about 2 m when the wind speed is 30 m/s. Assuming $H = 15$ m we find from formula (4) wave load $F_w = 61$ kN/m applied to JS from the seaside.

Waves can't penetrate inside cofferdam, where the water pressure is assumed almost hydrostatic during storms. The hydrostatic pressure causes the force $F_w = \rho_w g H_s^2 / 2 \approx 20$ kN/m applied to JS from inner side of cofferdams in case when sea level drops on 2 m on seaside of cofferdams.

CONCLUSIONS

The laser scanner survey performed in 2020 discovered significant deformation of the cofferdam constructions compared to the previous scan sessions performed in 2012-2015. The difference shows shifts up to 110 cm, which led to deflections and ruptures of metal reinforcing bars and joggle skirts. Over a year the quay is subjected to the influence of wave loads in ice-free season and ice loads in ice season. Thermal expansion of JS steel is determined by $CTE = 1.2 \cdot 10^{-5} K^{-1}$ of steels. It is smaller than CTE of fresh ice in 5 times. Thermal stresses in JS itself occur along the line of the confinement of JS between the piles, while thermal deformations of ice trapped inside cofferdams force bending deformations of JS.

Highest regular ice loads up to 0.6 MPa on JS from surface layer of ice trapped inside the cofferdam were registered in alongshore direction in winter season 2013. They were explained by negative thermal expansion of the ice at low tide (Marchenko, 2018). Maximal mechanical loads of ice trapped inside cofferdams are realized at low tide near the ice bottom. They were estimated below 0.25 MPa. The loads on JS from surface ice layer in onshore direction on the seaside of the cofferdam were mostly lower 50 kPa according to the measurements performed in 2013 and 2015 (Marchenko, 2018). Wave loads on JS in onshore direction were estimated in the same range. Thus, most significant loads on JS were from thermal expansion of ice trapped inside cofferdams.

In 2020 we measured compression stresses in the surface layer of ice near the seaside of the cofferdam. Maximal compressions above 60 kPa were measured in syzygy tide at the stage of low tide. The mean level of compression amplitudes varied around 30 kPa. Similar increase of ice pressure amplitude on JS from surface layer of ice trapped inside the cofferdam was registered in 2013. The thermal expansion of ice inside cofferdams was associated with inner heating and cooling of ice caused by regular migration of sea water though the ice under the influence of semidiurnal tidal pressure below the ice. We discovered that on the seaside of cofferdams sea water penetrates on the ice surface in high tide along JS. This process influence the heating of ice from the surface.

Numerical simulations were focused on qualitative investigation of the influence of water floods on the ice surface on thermal loads in sea and fresh ice. We investigated thermal behavior of ice sheet of 1 m thickness and 5 m length constrained between vertical walls. The simulations showed a range of ice pressure variations similar the measured pressures at the distance of 30-40 cm from the ice surface. It was discovered that maximal load of sea ice on the walls reached 0.17 kN/m over short time events occurred when the ice surface temperature changed with high rate. Simulated loads of fresh ice on the walls were much smaller.

We think that smaller distance between supporting piles (5.5 m) prevented bending deformation of JS on the seaside of cofferdams. Big bending deformations of JS in alongshore direction occurred between the piles extended on 10 m from each other. Dynamics and stability of seabed soil under the quay should be analyzed to estimate the influence of soil pressure on JS.

ACKNOWLEDGEMENTS

The work was supported by the Research Council of Norway through the IntPart project Arctic Offshore and Coastal Engineering in Changing Climate.

REFERENCES

Brown, J., Poirier, L., Frederking, R.M.W., 2019. Formation and Dynamics of an Ice Bustle at the Nanisivik Wharf. *POAC19-99*.

Caline, F., 2009. Coastal Sea Ice Conditions Around a Breakwater in a Microtidal, Inner-fjord River Delta in Svalbard (Ph.D. thesis), 221 pp.

Instanes, B., 1979. Coal loading pier in Svea, Svalbard. *Proc. of POAC-79*, 3, 217-227.

Kowalik, Z., Marchenko, A., Brazhnikov, D., Marchenko, N., 2015. Tidal currents in the western Svalbard Fjords. *Oceanologia*. 57, 318-327.

Marchenko, A., Shestov, A., Sigitov, A., Løset, S., 2011. Water-ice actions on the coal quay at Kapp Amsterdam in Svalbard. *POAC11-145*.

Marchenko A, Lishman B., 2017. The influence of closed brine pockets and permeable brine channels on the thermo-elastic properties of saline ice. *Phil.Trans. R. Soc. A* 375: 20150351.

Marchenko, A., 2018. Thermo-mechanical loads of confined sea ice on structures. *Phil.Trans. R. Soc. A* 376: 20170341.

Milano, V., 1973. Ship resistance to continuous motion in ice. *Trans. SNAME*, Vol. 81, 274-306.

Moslet, P. O., 2001. Estimation of loads exerted by sea ice on the quay at Kapp Amsterdam, the Van Mijen fjord. Master's thesis, Department of Structural Engineering, NTNU. 93 p.

Moslet, P. O., Høyland, K. V., 2003. Ice stress Measurements adjacent to a wide structure in land-fast ice. *Proc. of POAC-03*, Vol 1, 283-292.

Nazintcev, Yu. L., 1964. Some data for the calculation of thermal properties of sea ice. *Proceedings of the Arctic and Antarctic Research Institute*, Vol. 267. Gidrometeoizdat, Leningrad, pp. 31-47. (in Russian).

Oumeraci, H., Kortenhaus, A., Allsop, W., de Groot, M., Crouch, R., Vrijling, H., Voortman, H., 2001. "Probabilistic Design Tools for Vertical Breakwaters", Balkema Publishers, New York.

Poirier, L., Brown, J., Frederking, R., 2019. Environmental Monitoring and Ice Forces on the Nanisivik Wharf. *POAC19-89*.

Pounder ER. 1965 *The physics of ice*. Oxford, UK: Pergamon Press.

Renshaw, C. E., Marchenko, A., Schulson, E.M., Karulin, E., 2018. Effect of compressive loading on first-year sea-ice permeability. *J. Glaciology*, 64(245), 443-449.

Ryvlin, A.Ya., 1973. Experimental investigation of ice friction. *Proceedings of the Arctic and Antarctic Research Institute*, Vol. 309, 186-199.

Schwerdtfeger, P., 1963. The thermal properties of sea ice. *J. Glaciology*, 4 (36), 789-807.

Wrangborg, D., Marchenko, A., Murashkin, D., 2015. Measurement of load exerted by sea ice on the quay at Kapp Amsterdam on Svalbard. *POAC15-141*.